Borghei, Maryam; Baniasadi, Hossein; Abidnejad, Roozbeh; Ajdary, Rubina; Mousavihashemi, Seyedabolfazl; Robertson, Daria; Niskanen, Jukka; Kontturi, Eero; Kallio, Tanja; Rojas, Orlando J,

Wood flour and Kraft lignin enable air-drying of the nanocellulose-based 3D-printed structures

Published in:
Additive Manufacturing

DOI:
10.1016/j.addma.2024.104397

Published: 04/09/2024

Document Version
Publisher's PDF, also known as Version of record

Additive Manufacturing 92 (2024) 104397

Contents lists available at ScienceDirect

Additive Manufacturing

journal homepage: www.elsevier.com/locate/addma

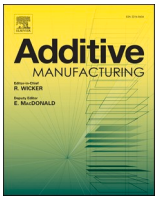

Wood flour and kraft lignin enable air-drying of the nanocellulose-based 3D-printed structures

Maryam Borghei [a,b,*], Hossein Baniasadi [c], Roozbeh Abidnejad [a], Rubina Ajdary [a], Seyedabolfazl Mousavihashemi [d,e], Daria Robertson [a], Jukka Niskanen [c], Eero Kontturi [a], Tanja Kallio [e], Orlando J. Rojas [a,f,*]

[a] Department of Bioproducts and Biosystems, School of Chemical Engineering, Aalto University, Aalto, 00076, Finland
[b] Department of Applied Physics, School of Science, Aalto University, Aalto, 00076, Finland
[c] Polymer Synthesis Technology, School of Chemical Engineering, Aalto University, Espoo, Finland
[d] VTT Technical Research Centre of Finland Ltd, P.O. Box 1000, Espoo 02044, Finland
[e] Department of Chemistry and Materials Science, Aalto University, Aalto, Espoo 00076, Finland
[f] Bioproducts Institute, Department of Chemical & Biological Engineering, Department of Chemistry, Department of Wood Science, 2360 East Mall, The University of British Columbia, Vancouver, BC V6T 1Z3, Canada

ARTICLE INFO

Keywords:
Cellulose
Wood flour
Kraft Lignin
Direct ink writing
Drying

ABSTRACT

The predominant technique for producing 3D-printed structures of nanocellulose involves freeze-drying despite its drawbacks in terms of energy consumption and carbon footprint. This study explores the less-energy-intensive drying approach by leveraging the valorization of forest residual streams. We utilized wood flour and Kraft lignin as fillers to facilitate room-temperature drying of the nanocellulose-based 3D printed structures. Various ink formulations, integrating cellulose nanofibers, wood flour, and lignin, were tested for direct ink writing (DIW). The formulations exhibited shear-thinning behavior and distinct yield stress with rising stress levels, ensuring the effective flow of the ink during DIW. Consequently, multilayered objects were printed with high shape fidelity and precise dimensions. Lignin and wood flour prevented structural collapse upon room-temperature drying. A reduced shrinkage was observed with the addition of lignin in freeze and room temperature drying. Moreover, the room-temperature dried samples were denser and demonstrated significantly higher resistance to applied compressive force, surpassing those reported for cellulose-based 3D composites in the existing literature. Remarkably, the trade-off effects of lignin are highlighted in terms of efficient stress-distributing and micro-scale sliding, enabling better strength. Along with wood flour, it further increases thermal stability. However, lignin hinders the hierarchical porous structure, the main ion transportation channels, reducing the double-layer capacitance of the carbonized structures. Overall, the results underscore the potential of all-biobased formulations for DIW for practical applications, highlighting their enhanced mechanical properties and structural integrity via the more sustainable drying method.

1. Introduction

Additive manufacturing, specifically 3D printing, is a technology that enables the creation of three-dimensional objects from digital models. There are several types of 3D printing approaches, each with advantages and applications. Material extrusion (ME) comprises a group of contact-based 3D printing methods where the material is systematically deposited to construct objects layer-by-layer [1–3]. ME techniques exhibit adaptability and are compatible with diverse materials, encompassing plastics, metals, ceramics, composites, and, in specific instances, bio-based materials. Several prevalent 3D printing methods fall within the ME classification, including fused deposition modeling, pellet extrusion, paste extrusion, and direct ink writing (DIW) [4,5]. The latter, DIW, uses liquid or viscous ink, often composed of a mixture of materials such as polymers, nanoparticles, or other functional components. The ink is extruded from a nozzle onto a substrate, forming the desired structure through controlled deposition. However, this technique has certain limitations related to the rheological properties of the

* Corresponding authors at: Department of Bioproducts and Biosystems, School of Chemical Engineering, Aalto University, Aalto, 00076, Finland.
E-mail addresses: maryam.borghei@aalto.fi (M. Borghei), orlando.rojas@ubc.ca (O.J. Rojas).

https://doi.org/10.1016/j.addma.2024.104397
Received 15 March 2024; Received in revised form 5 August 2024; Accepted 27 August 2024
Available online 31 August 2024

materials used. The viscosity of the ink is a critical factor in DIW, affecting the overall quality of the printed object [6–8]. Furthermore, some materials used in DIW may exhibit shear-thinning behavior with an increased shear rate. While DIW supports a wide range of materials, not all materials are suitable for the process. Inks with very high viscosity or rapid changes in viscosity under shear may pose challenges in achieving precise and consistent printing [9,10]. On the other hand, the drying issue post-3D printing of inks in DIW poses a significant challenge in terms of structural integrity and print quality [11].

Cellulose-based inks can be formulated to exhibit specific rheological properties suitable for DIW. Controlling viscosity and shear-thinning allows for precise extrusion and layer deposition during the printing process. As a result, cellulose-based inks have been used to create 3D structures [12–15]. Similar to most hydrogels, cellulose-based inks often contain a high proportion of water and require careful consideration of the drying processes, e.g., to prevent deformations and maintain the intended shape of the printed object. This is due to the shrinkage or volumetric changes of the hydrogel material upon drying.

Freeze drying or lyophilization after DIW is used to avoid the challenges of materials with high water content or solvents (minimizing shrinkage, deformation, or cracking). In fact, dried printed samples of high quality are not feasible without resorting to freeze-drying [16,17]. For instance, Baniasadi et al. [18] observed 83 % shrinkage in the cellulose-based printed sample when air-dried, while only 12 % shrinkage when subjected to freeze-drying. Additionally, inks comprising nanocellulose and xanthan gum recorded a substantial 90 % shrinkage during room drying, contrasting with a minimal 5 % shrinkage for the freeze-dried counterpart [19]. Moreover, it was noted that a considerable shrinkage along the Z-axis occurred for printed objects dried at 60 °C [20].

Liu et al. [21] utilized lignocellulose nanofiber (LCNF) derived from unbleached pulp for DIW printing. The LCNF ink, containing approximately 12 % residual lignin nanoparticles ranging from 14 to 40 nm, exhibited superior shape fidelity and mechanical properties in the 3D printed structures after freeze-drying, compared to those printed with bleached nanocellulose ink. However, they did not investigate the shrinkage of the samples in other drying conditions.

On the other hand, the positive effects of particles and fillers such as cellulose nanocrystals, silica nanoparticles, clays, and metal nanoparticles on ink stability and reinforcement of printed objects were observed [11,22,23]. Conversely, the shape and size of the fillers significantly impact ink stability and the reinforcement of printed and dried structures; for instance, smaller filler particles are less effective in reducing shrinkage after drying [24]. In a recent study on the effect of the shape of the fillers, Zhang et al. [25] demonstrated that incorporating micron-sized needle-like silk particles into a chitosan matrix enhances the modulus reinforcement of the printed structure compared to the inks containing spherical silk particles.

In this study, we decided to use needle-like wood flour (with an average size of 400 μm) to reinforce 3D printed structures with commonly used DIW ink containing TEMPO-oxidized cellulose nanofibrils (TOCNF). We also added methylcellulose to improve the adhesion of the wood flour to the nanocellulose fibers within the ink formulation. While previous research on 3D printing with wood powder has predominantly focused on material extrusion with wood powders mixed with polymeric binders (typically polylactic acid, and occasionally methylcellulose and gypsum) [26], a significant issue with DIW-printed objects is substantial shrinkage due to the high water content of the ink. Freeze-drying is generally a time-consuming process, and the sublimation step can take considerable time, depending on the size and complexity of the printed object. Furthermore, freezing and sublimation consume significant energy compared to other drying methods. Specifically, the energy consumption associated with freeze-drying raises environmental concerns, particularly in terms of its carbon footprint [27,28].

In our work, the addition of approximately 8 % wood flour to the TOCNF ink not only reduced shrinkage in the freeze-dried samples but also prevented collapse in samples dried at room temperature. This prompted us to investigate the addition of micron-sized fillers to our water-based ink to further minimize shrinkage, especially with room-drying methods. While additional wood flour led to clogging of the printing needle, the incorporation of spherical lignin particles (average size of 50–80 μm) effectively served as stress-distributing agents in the composite ink material. These spherical particles act as micro-scale 'sliding interfaces' under tensile stress, allowing the particles to redistribute and absorb forces more evenly across the material. Consequently, the presence of these spherical lignin particles significantly enhances the structural integrity of the sample, effectively mitigating fracture or breakage under tension [29]. Furthermore, our investigation encompassed a comprehensive characterization of the kraft lignin, ink rheology, drying techniques for the final specimens, morphological changes, and mechanical attributes. Specifically, we delved into the effects of different drying conditions—comparing freeze-drying (F-drying) and room-temperature drying (RT-drying)—on the 3D-printed samples, analyzing shape retention, microstructural attributes and the mechanical reinforcement exhibited by the dried scaffold. The printed samples were subjected to carbonization and implemented for double-layer capacitance.

2. Experimental

2.1. Materials

TEMPO-oxidized cellulose nanofibrils (TOCNF) were synthesized using the established procedure detailed in our prior works, employing never-dried bleached birch pulp as the source material [30,31]. Softwood kraft lignin powder (Indulin AT), with a composition of 3 % ash and 1.3 % sulfur, was procured from Mead Westvaco [32]. Methylcellulose (MC, viscosity 15 mPa.s) was sourced from Sigma Aldrich. Wood flour was derived by grinding birch wood and subsequently screening the resulting particles through a sieve with 0.4 mm mesh openings.

2.2. Methods

Ink preparation. The inks for DIW were prepared in accordance with Table 1. Our initial screening revealed that the maximum feasible concentration for printing TOCNF with our printer was 1.2 %. Consequently, this concentration remained constant in all formulations. The total mass of the dried polymer in the cellulose-based ink, comprising TOCNF and MC, was maintained at 1 %. Specifically, 0.66 g of MC was dissolved in 20 g of TOCNF (1.2 %). Conversely, the optimal quantity of wood flour, determined by considerations of printing quality and shape integrity post-drying, was twice the mass of the cellulose components. Subsequently, the influence of lignin was examined by adding 0.5 g and 1 g of lignin to the formulation. The formulations were designated as WL0, WL0.5, and WL1, respectively, denoting composites containing 0, 0.5, and 1 g of lignin. Two reference inks, denoted as T and TM, were printed, representing TOCNF and TOCNF/MC inks, respectively, without the inclusion of lignin and wood flour.

Direct ink writing. The inks were deposited using a BIOX bioprinter (CELLINK, Sweden) to construct the 3D model (g-code) designed *via*

Table 1
Summary of the ink compositions used in this work.

Ink	TOCNF (1.2 %) (g)	Methylcellulose (g)	Wood flour (g)	Lignin (g)
WL0	0.24	0.66	2	0
WL0.5	0.24	0.66	2	0.5
WL1	0.24	0.66	2	1
Reference inks				
T	0.24	0	0	0
TM	0.24	0.66	0	0

Tinkercad. Prior to printing, the inks were carefully loaded into 3 ml transparent pneumatic syringes, which were subsequently placed within a THINKY ARE-250 mixer to ensure homogeneity and eliminate bubbles. The printing process was facilitated using a 14 G tapered plastic nozzle (31.75 mm long, 1.5 mm outer diameter), with the printing speed set at a constant 10 $mm.s^{-1}$. Pneumatic pressures were adjusted in the range of 30–100 kPa, with higher pressures required for inks containing lignin and wood flour. The 3D structures were printed based on a rectangular lattice model (20 mm × 20 mm × 3 mm) with a 20 % infill density. For compression tests, disk-shaped samples (20 mm diameter and 3 mm height) with 50 % infill density were printed. Subsequently, the printed samples were dried in different drying conditions, i.e., freeze-drying (F-drying) and room-temperature drying (RT-drying). For F-drying, the samples were initially frozen at −18 °C and then subjected to drying under vacuum at −50 °C (Labconco 2.5). While for TR-drying, the sample was dried at 23 °C with 60 % humidity. The samples dried by freeze-drying were labeled as WL0-F, WL0.5-F, and WL1-F, while those obtained by room-temperature drying were designated as WL0-R, WL0.5-R, and WL1-R.

Lignin characterization. The chemical fingerprints of the kraft lignin were characterized by ATR-FTIR (Perkin Elmer-Spectrum Two FTIR Spectrometer). The size distribution of the lignin powder was determined by the laser diffraction method (Malvern-Mastersizer 2000). The device accepted range of the size distribution lies between 0.02 and 2000 μm, according to the laser diffraction. The measurements were repeated five times.

Rheology. The viscoelastic properties of the ink were examined through a series of rheological tests conducted using an Anton Paar Physica rheometer model MCR 301. The measurement was conducted at ambient temperature with the furnace kept closed to ensure that the rheological data was not affected by evaporation. To begin with, the trend of shear viscosity versus shear rate was charted, covering a wide range of shear rates from 0.01 1/s to 1000 1/s. This analysis was carried out utilizing a 25 mm cone and plate geometry with a precise gap size of 49 μm. Subsequently, a strain sweep test was executed, wherein shear strain exponentially increased from 0.01 % to 100 % while maintaining a constant angular frequency of 10 rad/s. The purpose of this test was to pinpoint the linear viscoelastic region of the ink. Subsequently, a frequency sweep test was conducted within the linear viscoelastic region at a fixed shear strain rate of 0.1 %, with the angular frequency ramped logarithmically from 0.01 to 640 rad/s. The evaluation of the ink yield stress (τ_y) involved conducting a stress sweep test, wherein stress levels escalated logarithmically from 0.1 to 10^3 Pa while maintaining a constant frequency of 10 rad/s. This evaluation was then combined with the maximum shear stress occurring within the nozzle (τ_{max}) and the shear rate at the nozzle wall. This comparison aimed to assess the flowability of the inks under specific conditions similar to the printing process. The inks were expected to exhibit successful printing characteristics if τ_{max} proved sufficiently high to surpass τ_y. To calculate τ_{max}, the following equation was employed [33].

$$\tau_{max} = \frac{\Delta P.r}{2L} \tag{1}$$

where ΔP represents the maximum pressure applied at the nozzle (30–100 kPa), while r and L denote the nozzle radius (1.5 mm) and length (31.75 mm), respectively.

τ_y was also calculated by fitting the steady shear data using the Herschel Bulkley model (Eq. 2), where K is the consistency index, $\dot{\gamma}^n$ is the shear rate, and n is the flow behavior index.

$$\tau = \tau_y + K\dot{\gamma}^n \tag{2}$$

Scanning electron microscopy. The morphology of the samples was analyzed using scanning electron microscopy (SEM) with a Zeiss Sigma VP electron microscope at an acceleration voltage of 3–5 kV. Prior to imaging, the samples were coated with a 4 nm layer of gold-palladium using a Leica EM ACE600 sputter coater.

Porosity. The porosity of the dried sample was determined by observing the mass variation of the sample when immersed in ethanol (Etax Aa, 99.5 %). The dried sample, possessing a specific apparent volume (V), was initially weighed (m_0). Subsequently, it was submerged in an ethanol solution for a duration of 2 hours. Following the immersion period, the sample was carefully retrieved from the ethanol solution, and after ensuring the removal of any residual surface ethanol, the sample was re-weighed (m_f). The porosity (φ) was then obtained using (Eq. (3)), in which ρ represents the density of ethanol (0.789 g/cm^3). Each sample underwent a minimum of three measurements, and the reported values represent the mean value ± Std. Dev.

$$\varphi(\%) = \frac{m_f - m_0}{\rho V} \times 100 \tag{3}$$

Shrinkage behavior of the 3D printed structures. The alterations in dimensions of the printed sample after drying were quantified as its shrinkage. The initial apparent volume of the sample was measured before (V_b), and the final apparent volume was determined after drying (V_a). The percentage shrinkage was then calculated using (Eq.(4))[14].

$$Shrinkage(\%) = \frac{V_b - V_a}{V_b} \times 100 \tag{4}$$

Thermogravimetric analysis. Thermogravimetric analysis (TGA) analysis was performed using the Netzsch STA 449 F3 Jupiter instrument. About 25 milligrams of each specimen were placed in an Aluminum oxide crucible and subsequently introduced into the experimental setup. The heating program was initially set to operate within a temperature range of 40–800 °C, with a consistent heating rate of 10 °C/min. Throughout the experiment, the heating chamber was continuously purged with nitrogen at a rate of 70 ml/min.

Compression test. The compression mechanical properties of the sample were assessed using a Universal Tester, specifically the Instron Model 4204. For this purpose, a disk-shaped sample with a 30 mm diameter was 3D printed and subsequently subjected to compression testing with a 5 kN load cell at a rate of 1 mm/min. The testing was conducted under controlled conditions of 23°C and 55 % relative humidity, following a 48-hour preconditioning period to stabilize the sample. A stress-strain curve was generated, and the compressive modulus and compressive strength at 30 % and 70 % strain were determined and compared. Each sample underwent a minimum of three measurements, and the reported values represent the mean value ± std. Dev.

Carbonization and electrochemical tests. The dried 3D scaffolds underwent carbonization at 900 °C for 60 minutes with a heating rate of 5 °C/min in a tube furnace (NBD-O1200–50IC) under nitrogen flow. The carbonized 3D scaffolds were configured into a three-electrode cell, serving as free-standing working electrodes, with a platinum mesh as the counter electrode and an Ag/AgCl reference electrode in a 1 M H_2SO_4 electrolyte. Electrochemical analysis was conducted using an Autolab PGSTAT12 potentiostat (EcoChemie, Netherlands) controlled by NOVA software. Cyclic voltammograms (CV) were recorded within a potential window from 0 to 1 V, and galvanostatic charge/discharge tests were performed at various current densities across the voltage range of 0–1 V. Electrochemical impedance spectroscopy (EIS) was executed at open circuit voltage over a frequency range of 0.01 Hz to 100 kHz.

3. Results and discussion

Rheological behavior of the all-biobased inks. The rheology measurement was performed to investigate the viscoelastic performance of the developed ink formulations and to examine their printability. The results are summarized in Fig. 1. As can be seen, all the formulations provided a non-Newtonian behavior over the applied shear rate, where the viscosity dropped more than two orders of magnitude upon sweeping share rate from 0.01 to 1000 1/s. This shear-thinning behavior

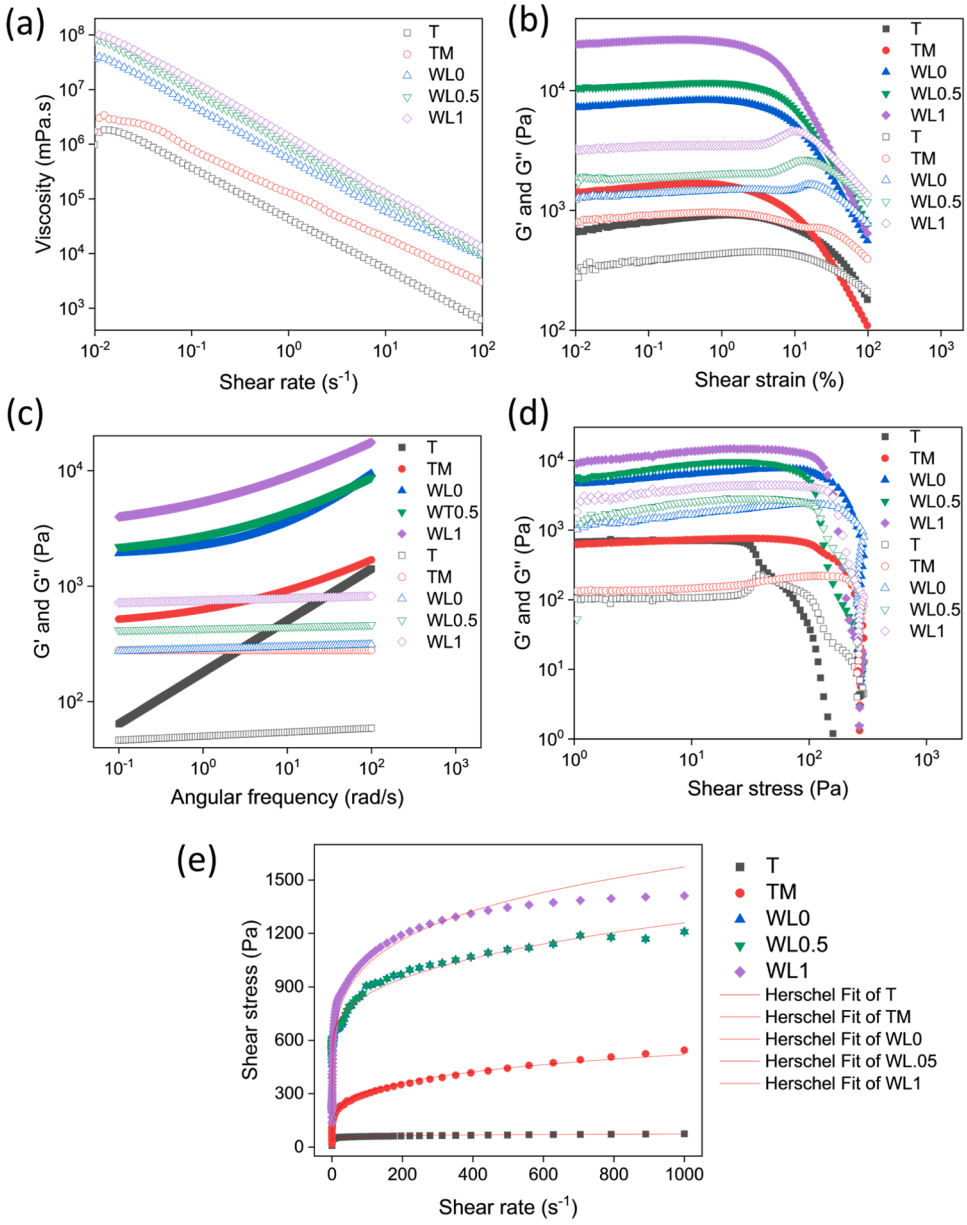

Fig. 1. Rheological properties of the all-biobased inks at 23 °C. a) Apparent viscosity versus share rate, b) strain sweep test results at a constant angular frequency of 10 rad/s, c) G′ and G″ versus shear stress at a fixed frequency of 10 rad/s, d) frequency sweep test results at a constant shear strain rate of 0.1 %, and f) The steady shear plots and the fitting curves using the Herschel-Bulkley model. The solid and blank symbols show G′ and G″, respectively. The frequency sweep test results were fitted non-linearly using the Herschel model due to the considerable variation observed in the data. The original curves are demonstrated in Fig. S1.

ensures the process works efficiently and produces high-quality prints. When the ink was at rest, all formulations exhibited viscosity values that were relatively high, aligning with those documented in the literature as suitable for DIW [34–38]. This sufficient viscosity prevents ink from flowing uncontrollably. However, upon increasing the shear rate, the viscosity reduced rapidly, suggesting that when extrusion was initiated, the ink flowed through the nozzle easily [39]. The formulations containing WL exhibit notably higher viscosity levels than those without. The difference in viscosity can be attributed to the higher concentrations of these formulations [40]. Additionally, an increase in viscosity was observed with the rising lignin content, primarily attributed to the formation of hydrogen bonds between lignin and cellulose. This interaction restricts mobility, consequently leading to an increase in viscosity [41].

The linear viscoelastic region was determined through a strain sweep test. As depicted in Fig. 1b, the moduli curves (G′ and G″) plateaued at a low deformation rate (less than 5 %), with G′ consistently surpassing G″. At higher strain rates, G″ intersected the G′ curve, indicating a flow point attributed to the yielding and destruction of the network structure. Consequently, a deformation magnitude of 0.1 % was chosen to ensure that the frequency sweep test remained within the linear viscoelastic region. The results of the frequency sweep test, shown in Fig. 1c, revealed that for all inks, G′ consistently exceeded G″, indicating solid or gel-like behavior under low shear strain. Moreover, both G′ and G″ exhibited an increase with rising lignin content, suggesting enhanced ink strength facilitated by hydrogen bond formation between the hydroxy and carboxyl groups of lignin and the hydroxyl groups of cellulose and wood flour.

Yield stress, τ_y, the point at which an ink transitions from a solid-like behavior to a more fluid-like behavior, is the minimum stress or force necessary to induce ink flow. As illustrated in Fig. 1d, when examining low shear rates, it becomes evident that G′ significantly surpassed G″ in all ink samples. This observation implies that the inks possessed notable

stability, allowing them to maintain their structural integrity within the nozzle even before the application of external pressure for the printing process [42,43]. As the applied stress was further increased beyond the linear viscoelastic range, we determined the yield stress point at the juncture where G′ intersected with G″, signifying the initiation of material flow from the nozzle. The values of τ_y exhibited a systematic increase with a higher proportion of lignin, a phenomenon possibly attributable to the reinforcing effect of lignin, as previously observed in the viscosity results. Conversely, we compared these τ_y values with τ_{max}, which represents the maximum shear stress generated within the nozzle. This value was determined to be in the range of 700–2000 Pa, (Eq. (1)). Notably, τ_{max} significantly exceeded the τ_y values of the inks, indicating that the applied pneumatic pressure exerted sufficient force to overcome the shear yield stress. Consequently, these findings suggest that all ink formulations can be effectively employed for DIW.

τ_y was also calculated by fitting the steady shear data using the Herschel-Bulkley model (Eq. (2)). The results are depicted in Fig. 1e, and the fitting parameters are summarized in Table 2. For comparison, τ_y values obtained from the stress sweep test curves (Fig. 1d) were also included. Notably, there is a difference between the yield stress values obtained from the steady shear plots and the stress sweep test curves. This discrepancy can be attributed to the different experimental conditions and methodologies used in each test. The stress sweep test measures yield stress based on the onset of flow under increasing stress, while the Herschel-Bulkley model fits the steady shear data over a range of shear rates, potentially leading to variations in the calculated yield stress. However, the yield stress values from curve fitting were still significantly lower than τ_{max}, indicating that the applied pneumatic pressure was sufficient to surpass the shear yield stress.

Printing and drying of the composites. We next explored the printing quality of the produced objects. As depicted in the upper section of Fig. 2a, the incorporation of lignin and wood flour into the WL formulation resulted in the formation of paste-like composites exhibiting a distinctive brownish color. The incorporation of lignin not only increased the ink consistency but also elevated its viscosity, as previously discussed. Notably, the ink with the highest lignin content denoted as WL1, exhibited a well-defined shear-thinning behavior, most likely explained by the dispersion ability of lignin. This property facilitated a smooth and continuous flow of the ink through the nozzle under applied pneumatic pressure, overcoming common challenges in DIW, such as needle clogging and liquid spreading. The inks, as depicted in Fig. 2b, demonstrated exceptional flowability, attributed to significantly lower yield stress values compared to the stress applied on the nozzle tip, in conjunction with their shear-thinning viscosity. Consequently, the achieved good printability exhibited high fidelity, fair resolution, and uniform filament diameter, showcasing precise control over the 3D-printed objects. Each layer maintained its individualized structure without collapse, ensuring a uniform and stable overall form.

The printed structures underwent drying under different conditions, namely Freeze drying and Room Temperature drying, to assess their impact on shape fidelity and overall structure. All printed scaffolds containing lignin and wood flour maintained their intended shapes without collapsing, as illustrated in Fig. 3. The presence of fillers influenced the appearance of the dried scaffolds, resulting in rougher surfaces, particularly in samples with higher wood flour and lignin content. In contrast, reference samples lacking fillers (T and TM) experienced collapse when dried at room temperature, retaining their shape fidelity only through freeze drying. Notably, methylcellulose played an effective role in binding nanocellulose fibers, contributing to a smoother surface on TM and retaining rectangular open spaces within the grid structure, contrary to samples containing only TOCNF. Furthermore, the inclusion of fillers had positive impact on preserving the geometry of the dried scaffold during room-temperature drying. The printed layers exhibited resilience, maintaining their individuality, and the corners retained rectangular angle despite experiencing higher shear tension during evaporation.

Comparing the dimensions of the samples, the shrinkage of the freeze-dried samples was minor and decreased with the higher lignin content, respectively, from 3.6 %± 1.4 (WL0-F), 3 % ± 0.6 (WL0.5-F) to 1.7 % ± 1 (WL1-F). The room-temperature dried samples shrank mainly along the Z-axis, respectively, from 31.9 ±8.8 % (WL0-RT), 24.7 % ± 1.5 (WL0.5-RT), to 10.8 % ± 3.6 (WL1-RT) when more lignin was added. This is attributed to the alignment tendency of wood flour, especially those with a higher aspect ratio, along the direction of printing.

Morphology and microstructure of the dried 3D-printed scaffolds. The morphology and microstructure of dried printed samples play a pivotal role in determining the overall quality, functionality, and performance of 3D-printed objects. Therefore, the microstructure of both F-dried and RT-dried samples was examined through SEM micrographs, presenting top views and cross-sections in Fig. 4. Notably, all samples exhibit rougher surfaces when compared to reference samples lacking wood and lignin. The F-dried sample without lignin (WL0-F) showcases a spongy and uniform porous structure, while the introduction of lignin results in a more heterogeneous structure with varied sizes and thicker walls. Top-view SEM images indicate that the RT-dried samples exhibit reduced grid width compared to the F-dried counterparts, which is attributed to shrinkage during room-temperature drying. Cross-section images reveal a denser, more tightly packed structure in RT-dried samples. Additionally, the introduction of lignin in both F-dried and RT-dried samples leads to more randomly dispersed structures due to the formation of aggregated lignin, as explained by the size distribution characterization (Figure S2).

Fig. 5 presents SEM images of WL0-F, WL0.5-F, and WL1-F with different resolutions. In the absence of lignin (WL0-F), the wood flour exhibits a distinct alignment along the printing direction induced by the shear from the nozzle. With increasing the lignin content, more aggregated lignin particles appeared and formed longer and more attached wood flour with longer lengths. The alignment of wood flour along the printing direction was also disturbed, resulting in a more heterogeneous pore structure. The higher lignin content also affects the positioning of the wood flour in different directions, including perpendicular to the printing direction, which contributes to holding the structure better in the Z-direction, consequently affecting the lower shrinkage in samples containing higher lignin content as observed in the previous section.

The porosity of the samples was determined by measuring the mass change of the samples when immersed in ethanol, a well-established method for assessing the porosity of porous materials [44,45]. While the material can absorb some ethanol, potentially affecting the weight, we took steps to minimize this effect by standardizing the immersion time for all samples and carefully removing any residual surface ethanol before re-weighing. Ethanol was chosen as the immersion medium due to its relatively low viscosity and high permeability, which enhance its ability to penetrate the porous structure while minimizing surface effects. However, isolated pores might not be fully saturated with ethanol; thus, we performed multiple measurements for each sample to account for variability and reported the mean value ± standard deviation to provide a measure of confidence in the results. As illustrated in Figure S3, porosity analysis is in correlation with the SEM observations, demonstrating lower porosity (approximately 10 %) for the RT-dried

Table 2
Summary of fitting parameters obtained by applying the Herschel-Bulkley model to the steady shear data.

Sample	τ_y (Pa)	K (Pa.s^n)	n Dimensionless	τ_y* (Pa)
T	10	43	0.07	39
TM	26	95	0.24	219
WL0	521	69	0.31	253
WL0.5	512	55	0.37	124
WL1	470	73	0.41	178

* Extracted from stress sweep curves

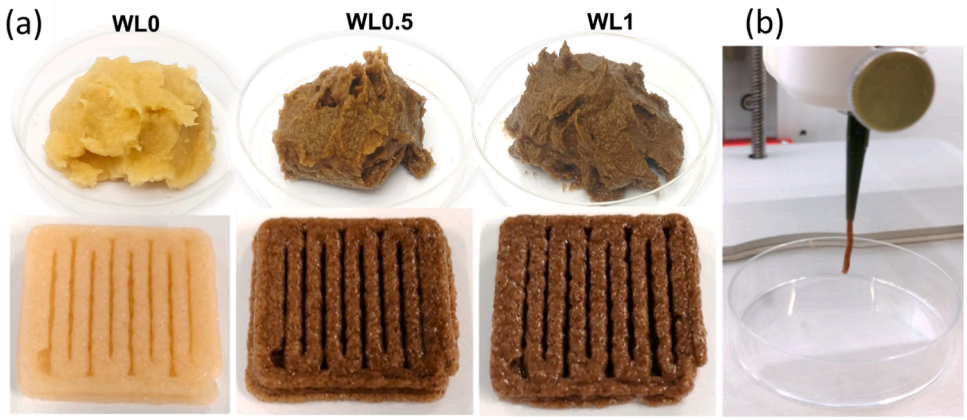

Fig. 2. Digital photographs of a) composite inks comprising lignin and wood flour, along with their corresponding 3D-printed objects, and b) the flowability of the ink from the nozzle.

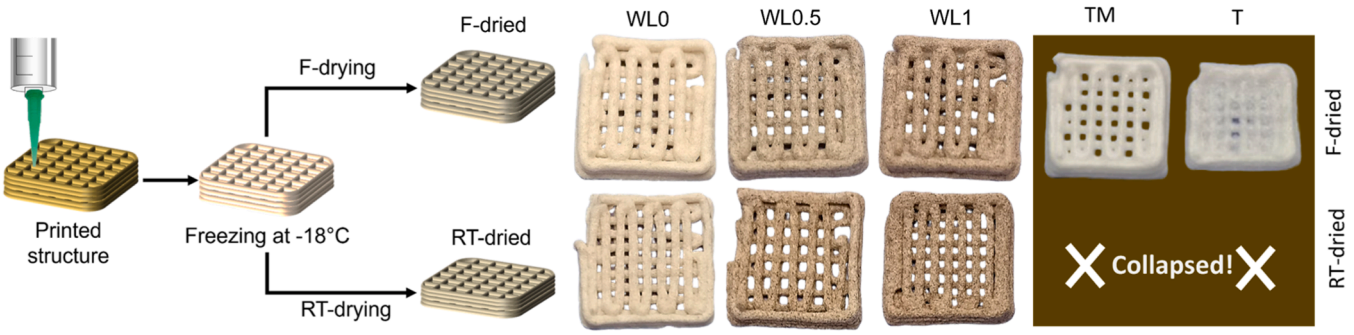

Fig. 3. a) Schematic illustration of DIW and drying methods after printing, b) Freeze-dried and room temperature-dried 3D-printed structures. Samples without filler, containing only TOCNF (T) and TOCNF-methylcellulose (TM), collapsed after room temperature drying and freeze-dried samples showed more shrinkage compared to those containing fillers.

samples compared to the F-dried samples (approximately 23 %). Freeze drying entails the sublimation of ice crystals, leaving behind a porous structure. This gentle drying process may yield a more open and porous network compared to room temperature drying, where solvent evaporation, such as water, occurs, potentially resulting in denser structures. Additionally, during freezing, ice crystals form within the sample matrix, which, upon sublimation during freeze-drying, can create void spaces, further enhancing porosity. However, porosity measurements reveal no significant differences between samples with varying lignin content. We will further apply electrochemical characterization to investigate the effect of lignin on porosity by correlation to the double-layer capacitance.

Mechanical strength. Compressive properties are vital for the overall structural integrity of printed objects. Objects subjected to compressive loads, such as columns, supports, and load-bearing components, must possess sufficient strength to withstand these forces without deformation or failure. Adequate compressive strength ensures that the parts can perform their intended functions without collapsing or deforming. Accordingly, the compressive mechanical properties of the printed samples (Figure S4) were measured and discussed. The typical stress-strain curves are plotted in Fig. 6a and b. Furthermore, the comparison of compressive modulus and compressive strength at 40 % and 70 % strain are provided in Fig. 6c and d. As illustrated, the compressive stress in all samples consistently increased with the applied force until reaching a strain of up to 95 %. Remarkably, none of the samples experienced failure during the test, indicating a highly robust 3D-printed structure. This resilience underscores the efficiency of the chosen ink formulation and 3D printing parameters, producing objects capable of withstanding applied forces without compromising their structural integrity. The successful completion of the test emphasizes the improved mechanical properties achieved through the incorporation of lignin and wood flour, contributing significantly to the overall strength and stability of the printed scaffolds.

This positive outcome holds promising implications for the potential utilization of these 3D-printed structures across various applications where mechanical durability and structural integrity are paramount considerations. Notably, with an increase in lignin content, almost all mechanical properties exhibit significant enhancement, suggesting the formation of more robust network structures. This improvement can be attributed to the effective interaction between cellulose and reinforcing particles, facilitated by hydrogen bonding between the hydroxy functionalities of cellulose and the hydroxyl and carboxyl functionalities of lignin (Figure S5) [46]. Moreover, lignin acts as a reinforcing filler in the cellulose matrix, increasing the material's resistance to deformation and enhancing its mechanical properties. This reinforcement effect can contribute to higher compressive strength and stiffness. Conversely, the RT-dried samples demonstrate notably higher mechanical performance, likely attributable to a more compact structure with reduced porosity achieved during the drying process. This observation highlights the influence of drying conditions on the mechanical characteristics of the printed structures.

It is noteworthy that the mechanical properties observed in our study surpass those reported for cellulose-based 3D composites in the existing literature. For instance, composite hydrogels of cellulose/polyacrylic acid displayed a maximum compressive strength of 350 kPa, accompanied by notably lower compressive modulus [47]. Additionally, a cellulose-based composite hydrogel designed for 3D printing applications exhibited compressive strength and modulus values of 0.4 MPa

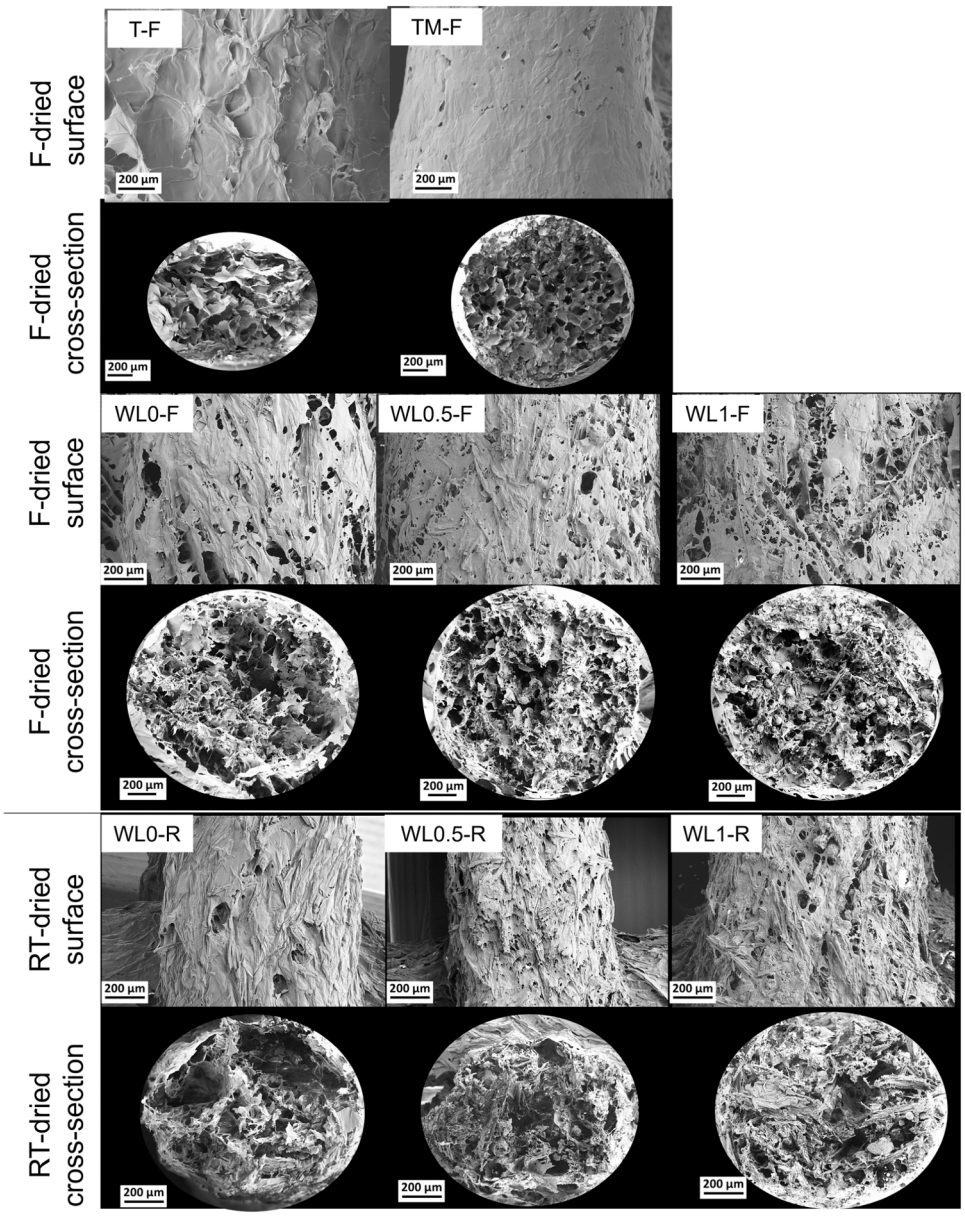

Fig. 4. The SEM micrographs from the top-view and cross-section perspectives of WL0, WL0.5, and WL1 subjected to drying processes *via* F-drying *vs.* RT-drying. The reference samples without fillers (T and TM) collapsed after RT-drying, thus, SEM micrographs are presented only for the F-dried samples.

and 1 MPa, respectively [48]. In comparison, Li et al. [49] reported a peak compressive strength of 1.8 MPa for alginate/gelatin/cellulose nanocrystals interpenetrating polymer network composite hydrogels, with a compressive modulus of less than 2 MPa. Furthermore, the self-assembled cellulose nanocrystals/chitosan nanobubbles composite hydrogel demonstrated the highest compressive strength, reaching 0.89 MPa [50]. Altogether, these findings contribute valuable insights into optimizing both material composition and drying methods for achieving superior mechanical properties in 3D-printed objects, expanding their potential applications across diverse areas.

Electrochemical behavior. The samples were carbonized to explore the impact of drying and lignin content on the double-layer capacitance, which correlates with the porous microstructure. Before carbonization, to understand the thermal characteristics of each material within the composition, the thermal stability of specimens was studied *via* thermogravimetric analysis (TGA), which can be seen in Figure S6.

As previously noted, room temperature drying proved advantageous in obtaining structures with higher mechanical properties, albeit at the cost of increased porosity loss. Carbonized RT-dried samples lacking significant double-layer capacitance were excluded from the presentation of this study. Electrochemical capacitance was measured for the carbonized F-dried samples in 1 M H_2SO_4, and the cyclic voltammograms (CV) are depicted in Fig. 7. All CV curves exhibit a quasi-rectangular shape in the three-electrode cell assembly at a scan rate of 100 mV/s, indicative of governing double-layer capacitance (Fig. 7a). Pseudo-capacitance behavior at low potentials is linked to the presence of functional groups (-OH, -CO, and -COOH) on carbon materials in acidic electrolytes. Analysis of CV measurements at different scan rates reveals that the double-layer capacitance decreases by increasing lignin content from WL0-FC to WL0.5-FC and WL1-FC (Fig. 7b). Fig. 7C shows galvanostatic charge-discharge (GCD) curves at different current densities. Electrochemical impedance spectroscopy (EIS) results (Fig. 7d) corroborated the CV findings, showing that WL0-FC boasts higher electrical conductivity (high-frequency intercept of EIS data). At low frequencies, the proximity to a vertical line underscored the higher capacitive behavior of the WL0-FC sample compared to the other two

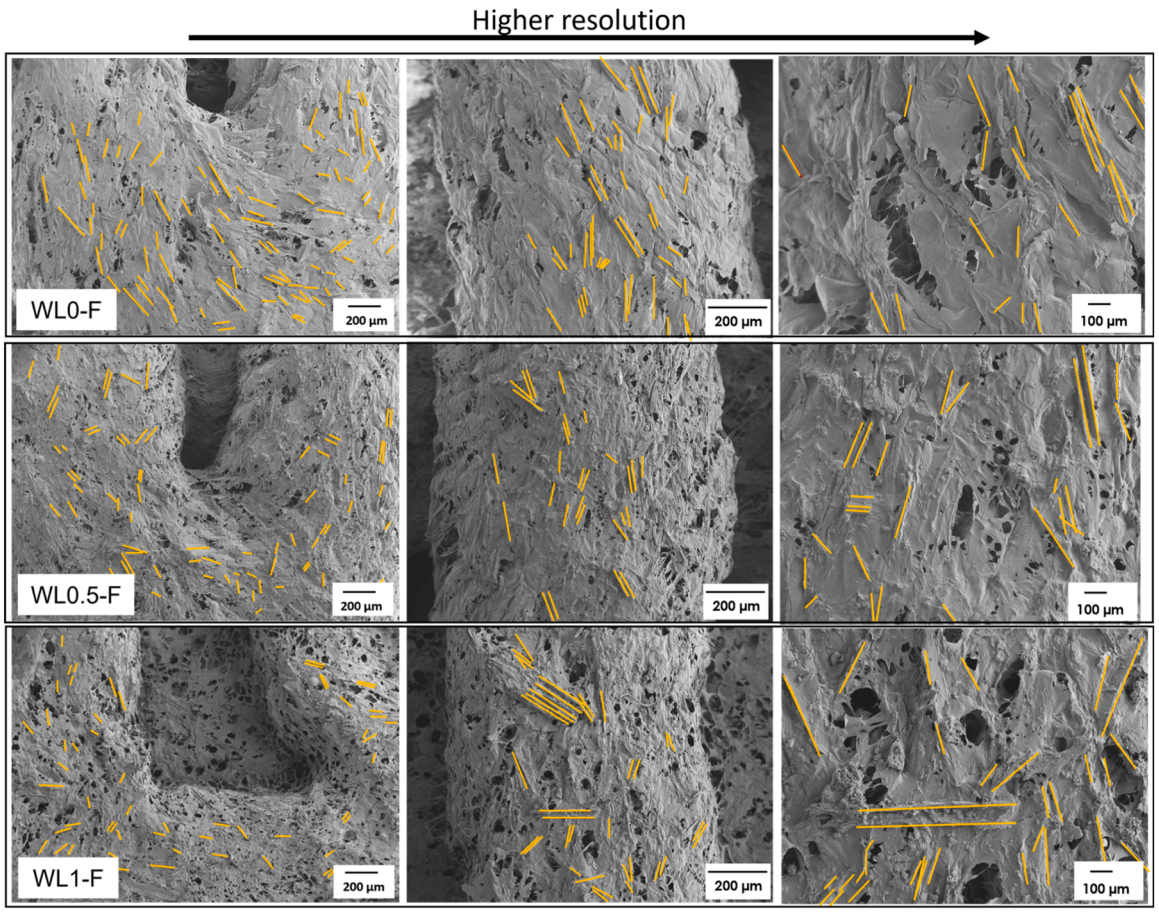

Fig. 5. SEM micrographs showing the alignment of the wood flour in WL0, WL0.5, and WL1 in different resolutions. Higher lignin content disturbed the alignment of wood flour along the printing direction.

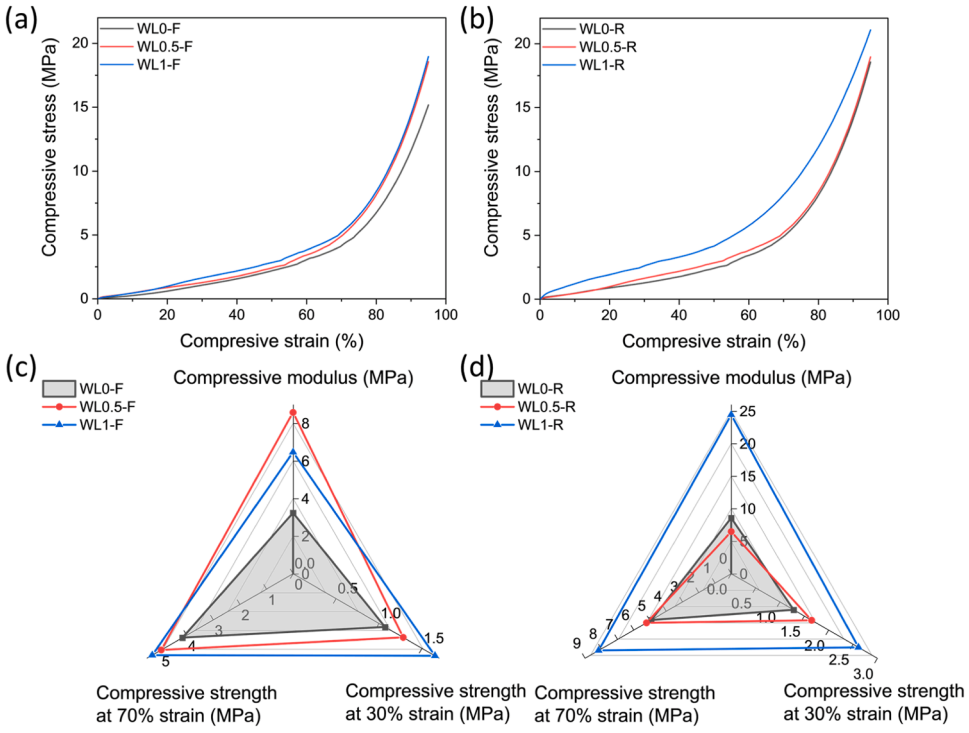

Fig. 6. a) and b) Typical compressive stress and strain curves. c) and d) Comparison of some mechanical properties extracted from stress-strain curves.

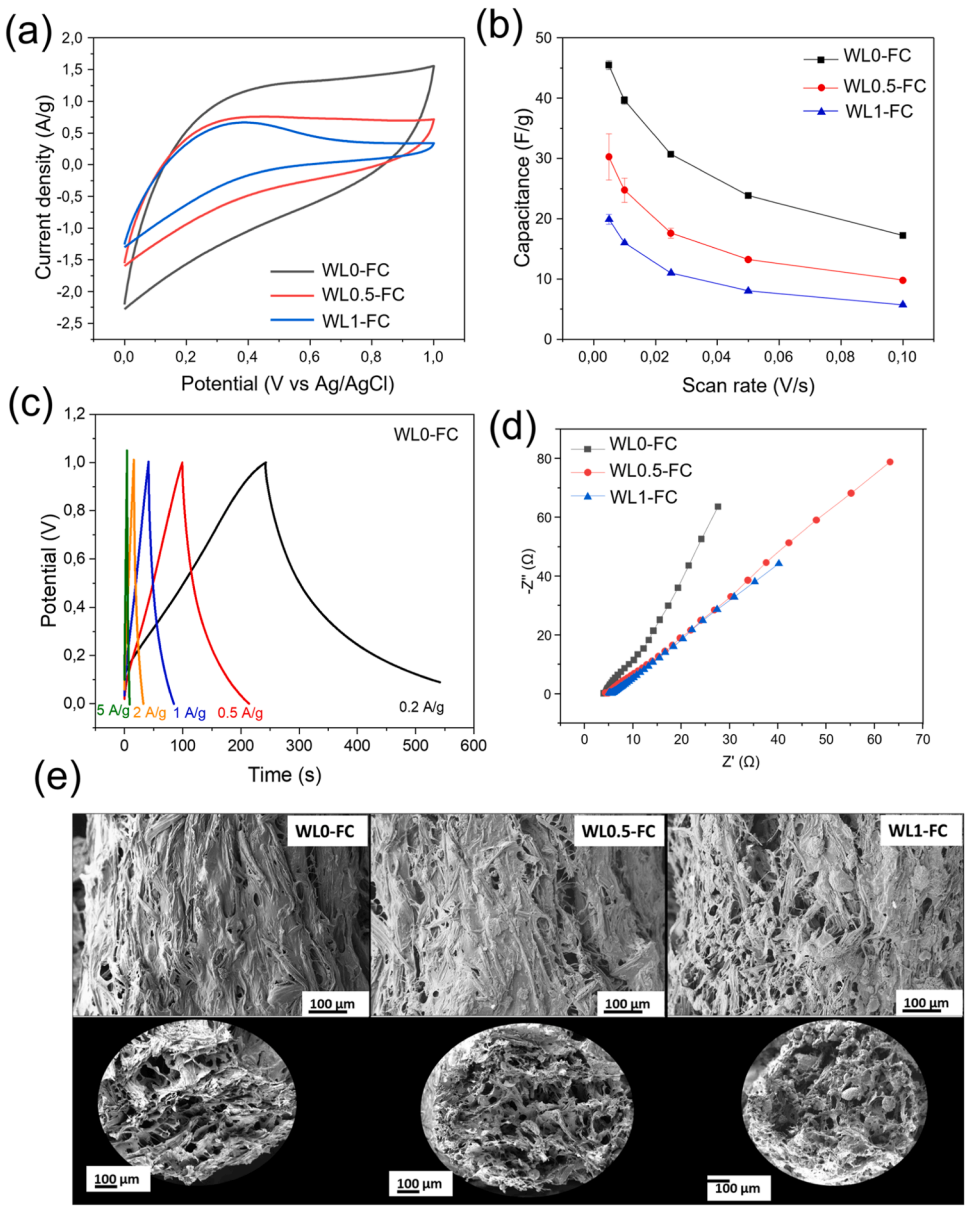

Fig. 7. Electrochemical measurements of carbonized (F-dried) samples in a three-electrode system. a) Cyclic voltammograms at the scan rates of 100 mV/s, b) Capacitance samples at different scan rates of 5–100 mV/s, c) GCD curves and specific capacitance of the WL0-FC sample at the current densities of 0.2–5 A/g, and d) Nyquist plots of the samples at the open-circuit potential, e) SEM images (top-view and cross-section) of the F-dried structures after carbonization used for super capacitance tests.

samples with more lignin [51,52]. These data suggest that the pore-blocking effect of lignin (in WL0.5-FC and WL1-FC) was more impactful in conductivity and electrochemical behavior than the increased carbon content after carbonization (TGA data). These findings align with SEM observations (Fig. 7e), indicating that the addition of more lignin hindered the hierarchical porous structure, which are the main transportation channels for ions to access smaller pores, consequently reducing double-layer capacitance. Similar behavior was observed in previous work on carbon fibers composed of lignin/TOCNF, where higher lignin content led to decreased double-layer capacitance [30]. Overall, the observations suggest that adding lignin to the cellulose-wood structure can be alternatively decided based on the final application, whether one desires higher mechanical properties or more porous structures.

4. Conclusions

This study provided valuable insights into the positive impact of kraft lignin and wood flour on reinforcing 3D-printed cellulose-based structures. The development and utilization of all-biobased ink formulations demonstrated promising results in terms of rheological properties and printability. The observed shear-thinning viscosity and distinct yield stress across all formulations ensured the effective flow of the ink during the 3D printing process, resulting in the successful production of objects with high shape fidelity and precise dimensions. The exploration of drying techniques, including freeze-drying and room-temperature drying, revealed that the presence of wood flour and lignin allowed for room-temperature drying without significant structural collapse. The room-temperature dried structures exhibited comparable characteristics to those obtained through standard freeze-drying methods but with reduced porosity and denser structures at the Z-axis, as confirmed by SEM imaging and porosity results. Notably, the room-temperature dried

samples demonstrated significantly higher mechanical stability against applied compressive force, further emphasizing the potential practical applications of these structures. Finally, by carbonizing the printed structures, we investigated the influence of lignin on the microporous structure and the subsequent double-layer capacitance. Though the higher lignin content enhanced the mechanical properties, an adverse effect was observed on the microporous structure, likely by blocking the ion transport channels.

CRediT authorship contribution statement

Eero Kontturi: Writing – review & editing, Supervision, Funding acquisition. **Tanja Kallio:** Writing – review & editing, Supervision, Funding acquisition. **Orlando Rojas:** Writing – review & editing, Supervision, Resources, Funding acquisition. **Maryam Borghei:** Writing – review & editing, Writing – original draft, Visualization, Validation, Project administration, Methodology, Investigation, Funding acquisition, Formal analysis, Data curation, Conceptualization. **Hossein Baniasadi:** Writing – review & editing, Writing – original draft, Visualization, Formal analysis, Data curation. **Roozbeh Abidnejad:** Writing – review & editing, Writing – original draft, Formal analysis, Data curation. **Rubina Ajdary:** Writing – review & editing, Methodology, Data curation, Conceptualization. **Seyedabolfazl Mousavihashemi:** Writing – review & editing, Formal analysis, Data curation. **Daria Robertson:** Data curation. **Jukka Niskanen:** Resources, Funding acquisition.

Declaration of Competing Interest

The authors declare that they have no known competing financial interests or personal relationships that could have appeared to influence the work reported in this paper.

Data Availability

Data will be made available on request.

Acknowledgment

This project has received funding from the European Union's Horizon 2020 research and innovation program under grant agreement No. 760876 (INNPAPER project) and the ERC Advanced Grant Agreement No. 788489, "BioElCell". This work was a part of the Academy of Finland's Flagship Programme under Projects Nos. 318890 and 318891 (Competence Center for Materials Bioeconomy, FinnCERES). The Canada Excellence Research Chair Program (CERC-2018–00006) and Canadian Foundation for Innovation (CFI) are gratefully acknowledged (OJR). M.B. acknowledges Magnus Ehrnrooth Foundation for funding the CarboCat project. H.B. acknowledges the funding of the Research Council of Finland: No. 327248 (ValueBiomat). The authors acknowledge the provision of facilities and technical support by Aalto University at OtaNano, Nanomicroscopy Center (Aalto-NMC), and Aalto University Bioeconomy Facilities.

Appendix A. Supporting information

Supplementary data associated with this article can be found in the online version at doi:10.1016/j.addma.2024.104397.

References

[1] F. Zhang, L. Zhu, Z. Li, S. Wang, J. Shi, W. Tang, N. Li, J. Yang, The recent development of vat photopolymerization: a review, Addit. Manuf. 48 (2021) 102423, https://doi.org/10.1016/j.addma.2021.102423.
[2] Y. Yan, Y. Jiang, E.L.L. Ng, Y. Zhang, C. Owh, F. Wang, Q. Song, T. Feng, B. Zhang, P. Li, X.J. Loh, S.Y. Chan, B.Q.Y. Chan, Progress and opportunities in additive manufacturing of electrically conductive polymer composites, Mater. Today Adv. 17 (2023) 100333, https://doi.org/10.1016/j.mtadv.2022.100333.
[3] H. Chen, Y. Sun, W. Yuan, S. Pang, W. Yan, Y. Shi, A review on discrete element method simulation in laser powder bed fusion additive manufacturing, Chin. J. Mech. Eng. Addit. Manuf. Front. 1 (2022) 100017, https://doi.org/10.1016/j.cjmeam.2022.100017.
[4] D. Behera, M. Cullinan, Current challenges and potential directions towards precision microscale additive manufacturing – Part I: Direct ink writing/jetting processes, Precis. Eng. 68 (2021) 326–337, https://doi.org/10.1016/j.precisioneng.2020.12.009.
[5] T. Agarwal, M. Costantini, T.K. Maiti, Extrusion 3D printing with Pectin-based ink formulations: recent trends in tissue engineering and food manufacturing, Biomed. Eng. Adv. 2 (2021) 100018, https://doi.org/10.1016/j.bea.2021.100018.
[6] D.A. Rau, C.B. Williams, M.J. Bortner, Rheology and printability: a survey of critical relationships for direct ink write materials design, Prog. Mater. Sci. 140 (2023) 101188, https://doi.org/10.1016/j.pmatsci.2023.101188.
[7] Y. Cheng, Y. Fu, L. Ma, P.L. Yap, D. Losic, H. Wang, Y. Zhang, Rheology of edible food inks from 2D/3D/4D printing, and its role in future 5D/6D printing, Food Hydrocoll. 132 (2022) 107855, https://doi.org/10.1016/j.foodhyd.2022.107855.
[8] H. Baniasadi, R. Abidnejad, M. Fazeli, J. Lipponen, J. Niskanen, E. Kontturi, J. Seppälä, O.J. Rojas, Innovations in hydrogel-based manufacturing: a comprehensive review of direct ink writing technique for biomedical applications, Adv. Colloid Interface Sci. 324 (2024) 103095, https://doi.org/10.1016/j.cis.2024.103095.
[9] R.Y. Tay, Y. Song, D.R. Yao, W. Gao, Direct-ink-writing 3D-printed bioelectronics, Mater. Today (2023), https://doi.org/10.1016/j.mattod.2023.09.006.
[10] L. del-Mazo-Barbara, M.-P. Ginebra, Rheological characterisation of ceramic inks for 3D direct ink writing: a review, J. Eur. Ceram. Soc. (2021).
[11] N.R.M. Lévaro, M.F.R.P. Alves, C. Santos, V. Sencadas, S. Olhero, Direct ink writing of ATZ composites based on inks prepared by colloidal or hydrogel route: Linking inks rheology with mechanical properties, Colloids Surf. A Physicochem. Eng. Asp. 668 (2023) 131426, https://doi.org/10.1016/j.colsurfa.2023.131426.
[12] H. Taneja, S.M. Salodkar, A. Singh Parmar, S. Chaudhary, Hydrogel based 3D printing: Bio ink for tissue engineering, J. Mol. Liq. 367 (2022) 120390, https://doi.org/10.1016/j.molliq.2022.120390.
[13] S. Mallakpour, M. Tukhani, C.M. Hussain, Recent advancements in 3D bioprinting technology of carboxymethyl cellulose-based hydrogels: utilization in tissue engineering, Adv. Colloid Interface Sci. 292 (2021) 102415, https://doi.org/10.1016/j.cis.2021.102415.
[14] H. Baniasadi, R.T. Polez, E. Kimiaei, Z. Madani, O.J. Rojas, M. Österberg, J. Seppälä, 3D printing and properties of cellulose nanofibrils-reinforced quince seed mucilage bio-inks, Int. J. Biol. Macromol. (2021).
[15] P. Singh, H. Baniasadi, S. Gupta, R. Ghosh, S. Shaikh, J. Seppälä, A. Kumar, 3D-printed cellulose nanocrystals and gelatin scaffolds with bioactive cues for regenerative medicine: Advancing biomedical applications, Int. J. Biol. Macromol. (2024) 134402, https://doi.org/10.1016/j.ijbiomac.2024.134402.
[16] V.C.-F.F. Li, C.K. Dunn, Z. Zhang, Y. Deng, H.J. Qi, Direct ink write (diw) 3d printed cellulose nanocrystal aerogel structures, Sci. Rep. 7 (2017) 8018, https://doi.org/10.1038/s41598-017-07771-y.
[17] E. Erfanian, R. Moaref, R. Ajdary, K.C. Tam, O.J. Rojas, M. Kamkar, U. Sundararaj, Electrochemically synthesized graphene/TEMPO-oxidized cellulose nanofibrils hydrogels: highly conductive green inks for 3D printing of robust structured EMI shielding aerogels, Carbon N. Y 210 (2023) 118037, https://doi.org/10.1016/j.carbon.2023.118037.
[18] H. Baniasadi, R. Ajdary, J. Trifol, O.J. Rojas, J. Seppälä, Direct ink writing of aloe vera/cellulose nanofibrils bio-hydrogels, Carbohydr. Polym. (2021) 118114.
[19] H. Baniasadi, E. Kimiaei, R.T. Polez, R. Ajdary, O.J. Rojas, M. Österberg, J. Seppälä, High-resolution 3D printing of xanthan gum/nanocellulose bio-inks, Int. J. Biol. Macromol. 209 (2022) 2020–2031.
[20] C. Wang, S. Ma, D. Li, J. Zhao, H. Zhou, D. Wang, C. Liu, S. Wang, C. Chen, Direct ink writing of thermoresistant, lightweight composite polyimide honeycombs with tunable X-band electromagnetic wave absorption properties, Addit. Manuf. 70 (2023) 103554, https://doi.org/10.1016/j.addma.2023.103554.
[21] C. Liu, M.-C. Li, X. Liu, G. Zhou, C. Liu, C. Mei, 3D printing of customized lignocellulose nanofibril aerogels for efficient thermal insulation, Addit. Manuf. 78 (2023) 103841, https://doi.org/10.1016/j.addma.2023.103841.
[22] C.J.C. Nocheseda, F.P. Liza, K.A.M. Collera, E.B. Caldona, R.C. Advincula, 3D printing of metals using biodegradable cellulose hydrogel inks, Addit. Manuf. 48 (2021) 102380, https://doi.org/10.1016/j.addma.2021.102380.
[23] J. Vadillo, I. Larraza, T. Calvo-Correas, N. Gabilondo, C. Derail, A. Eceiza, Bioactive inks suitable for 3D printing based on waterborne polyurethane urea, cellulose nanocrystals and Salvia extract, React. Funct. Polym. 175 (2022) 105286, https://doi.org/10.1016/j.reactfunctpolym.2022.105286.
[24] W. Xu, S. Jambhulkar, Y. Zhu, D. Ravichandran, M. Kakarla, B. Vernon, D.G. Lott, J.L. Cornella, O. Shefi, G. Miquelard-Garnier, Y. Yang, K. Song, 3D printing for polymer/particle-based processing: a review, Compos. Part B Eng. 223 (2021) 109102, https://doi.org/10.1016/j.compositesb.2021.109102.
[25] J. Zhang, B.J. Allardyce, R. Rajkhowa, S. Kalita, R.J. Dilley, X. Wang, X. Liu, Silk particles, microfibres and nanofibres: a comparative study of their functions in 3D printing hydrogel scaffolds, Mater. Sci. Eng. C. 103 (2019) 109784.
[26] A.K. Das, D.A. Agar, M. Rudolfsson, S.H. Larsson, A review on wood powders in 3D printing: processes, properties and potential applications, J. Mater. Res. Technol. 15 (2021) 241–255, https://doi.org/10.1016/j.jmrt.2021.07.110.
[27] V. Prosapio, I. Norton, I. De Marco, Optimization of freeze-drying using a Life cycle assessment approach: strawberries' case study, J. Clean. Prod. 168 (2017) 1171–1179, https://doi.org/10.1016/j.jclepro.2017.09.125.

[28] C. Ertekin, T. Aktas, I. Alibas, H. Essalhi, in: S.M. Jafari, N.B.T.-D.T. in F. P. Malekjani (Eds.), 15 - Drying of fruits and vegetables, Woodhead Publishing, 2023, pp. 491–542, https://doi.org/10.1016/B978-0-12-819895-7.00004-3.
[29] X. Zhang, M. Morits, C. Jonkergouw, A. Ora, J.J. Valle-Delgado, M. Farooq, R. Ajdary, S. Huan, M. Linder, O. Rojas, M.H. Sipponen, M. Österberg, Three-dimensional printed cell culture model based on spherical colloidal lignin particles and cellulose nanofibril-alginate hydrogel, Biomacromolecules 21 (2020) 1875–1885, https://doi.org/10.1021/acs.biomac.9b01745.
[30] L. Wang, M. Borghei, A. Ishfaq, P. Lahtinen, M. Ago, A.C. Papageorgiou, M. J. Lundahl, L.-S. Johansson, T. Kallio, O.J. Rojas, Mesoporous carbon microfibers for electroactive materials derived from lignocellulose nanofibrils, ACS Sustain. Chem. Eng. 8 (2020) 8549–8561.
[31] G. Reyes, R. Ajdary, M.R. Yazdani, O.J. Rojas, Hollow filaments synthesized by dry-jet wet spinning of cellulose nanofibrils: structural properties and thermoregulation with phase-change infills, ACS Appl. Polym. Mater. 4 (2022) 2908–2916.
[32] B.L. Tardy, J.J. Richardson, J. Guo, J. Lehtonen, M. Ago, O.J. Rojas, Lignin nano- and microparticles as template for nanostructured materials: formation of hollow metal-phenolic capsules, Green. Chem. 20 (2018) 1335–1344.
[33] H. Baniasadi, Z. Madani, R. Ajdary, O.J. Rojas, J. Seppälä, Ascorbic acid-loaded polyvinyl alcohol/cellulose nanofibril hydrogels as precursors for 3D printed materials, Mater. Sci. Eng. C. 130 (2021) 112424, https://doi.org/10.1016/j.msec.2021.112424.
[34] K. Bouzidi, D. Chaussy, A. Gandini, E. Flahaut, R. Bongiovanni, D. Beneventi, Bio-based formulation of an electrically conductive ink with high potential for additive manufacturing by direct ink writing, Compos. Sci. Technol. 230 (2022) 109765, https://doi.org/10.1016/j.compscitech.2022.109765.
[35] P.T. Smith, A. Basu, A. Saha, A. Nelson, Chemical modification and printability of shear-thinning hydrogel inks for direct-write 3D printing, Polym. (Guildf.) 152 (2018) 42–50.
[36] A. Cianciosi, J. Simon, M. Bartolf-Kopp, H. Grausgruber, T.R. Dargaville, A. Forget, J. Groll, T. Jungst, M. Beaumont, Direct ink writing of multifunctional nanocellulose and allyl-modified gelatin biomaterial inks for the fabrication of mechanically and functionally graded constructs, Carbohydr. Polym. 319 (2023) 121145, https://doi.org/10.1016/j.carbpol.2023.121145.
[37] T. Wang, Z. Yu, J. Si, L. Liu, X. Ren, G. Gao, Gum arabic-based three-dimensional printed hydrogel for customizable sensors, Int. J. Biol. Macromol. 254 (2024) 128072, https://doi.org/10.1016/j.ijbiomac.2023.128072.
[38] J. Karvinen, M. Kellomäki, Design aspects and characterization of hydrogel-based bioinks for extrusion-based bioprinting, Bioprinting 32 (2023) e00274, https://doi.org/10.1016/j.bprint.2023.e00274.
[39] K. Enoch, R.C.S., A.A. Somasundaram, Improved mechanical properties of Chitosan/PVA hydrogel – a detailed Rheological study, Surf. Interfaces 41 (2023) 103178, https://doi.org/10.1016/j.surfin.2023.103178.
[40] S.W.A. Shah, Q. Xu, M.W. Ullah, S. Zahoor, G.M. Sethupathy, J. Morales, D. Sun, Zhu, Lignin-based additive materials: a review of current status, challenges, and future perspectives, Addit. Manuf. 74 (2023) 103711, https://doi.org/10.1016/j.addma.2023.103711.
[41] W. Feng, Z. Wang, Shear-thinning and self-healing chitosan-graphene oxide hydrogel for hemostasis and wound healing, Carbohydr. Polym. 294 (2022) 119824, https://doi.org/10.1016/j.carbpol.2022.119824.
[42] Z. Xu, Q. Zhang, C. Fan, M. Xiao, R. Yang, Y. Yao, Y. Wu, X. Nie, H. Wang, W. Liu, A gel microparticle-based self-thickening strategy for 3D printing high-modulus hydrogels skeleton cushioned with PNAGA hydrogel mimicking anisotropic mechanics of meniscus, Bioact. Mater. 26 (2023) 64–76, https://doi.org/10.1016/j.bioactmat.2023.02.020.
[43] H. Wang, C. Wu, J. Zhu, Y. Cheng, Y. Yang, S. Qiao, B. Jiao, L. Ma, Y. Fu, H. Chen, H. Dai, Y. Zhang, Stabilization of capsanthin in physically-connected hydrogels: Rheology property, self-recovering performance and syringe/screw-3D printing, Carbohydr. Polym. 319 (2023) 121209, https://doi.org/10.1016/j.carbpol.2023.121209.
[44] W. Zhang, W. Zhu, S. Shi, N. Hu, Y. Suo, J. Wang, Bioinspired foam with large 3D macropores for efficient solar steam generation, J. Mater. Chem. A. 6 (2018) 16220–16227.
[45] H. Pan, D. Fan, Z. Duan, C. Zhu, R. Fu, X. Li, Non-stick hemostasis hydrogels as dressings with bacterial barrier activity for cutaneous wound healing, Mater. Sci. Eng. C. 105 (2019) 110118.
[46] M.N.M. Ibrahim, A. Iqbal, C.C. Shen, S.A. Bhawani, F. Adam, Synthesis of lignin based composites of TiO2 for potential application as radical scavengers in sunscreen formulation, BMC Chem. 13 (2019) 1–14, https://doi.org/10.1186/S13065-019-0537-3/FIGURES/20.
[47] Y. Tian, L. Zhang, X. Li, M. Yan, Y. Wang, J. Ma, Z. Wang, Compressible, anti-freezing, and ionic conductive cellulose/polyacrylic acid composite hydrogel prepared via AlCl3/ZnCl2 aqueous system as solvent and catalyst, Int. J. Biol. Macromol. 253 (2023) 126550, https://doi.org/10.1016/j.ijbiomac.2023.126550.
[48] R. Vel, A. Bhatt, A. Priyanka, A. Gauthaman, V. Anilkumar, A.S. Safeena, R. S, DEAE- Cellulose-based composite hydrogel for 3D printing application: physicochemical, mechanical, and biological optimization, Mater. Today Commun. 33 (2022) 104335, https://doi.org/10.1016/j.mtcomm.2022.104335.
[49] Z. Li, H. Liu, Y. Liao, H. Wang, X. Sun, X. Chen, H. Yan, Q. Lin, Design and properties of alginate/gelatin/cellulose nanocrystals interpenetrating polymer network composite hydrogels based on in situ cross-linking, Eur. Polym. J. 201 (2023) 112556, https://doi.org/10.1016/j.eurpolymj.2023.112556.
[50] M. Javed, H. Huang, Y. Ma, F. Ettoumi, L. Wang, Y. Xu, H.R. El-Seedi, Q. Ru, Z. Luo, Construction of self-assembled nano cellulose crystals/chitosan nanobubbles composite hydrogel with improved gallic acid release property, Food Chem. 438 (2024) 137948, https://doi.org/10.1016/j.foodchem.2023.137948.
[51] L. Yang, Y. Feng, M. Cao, J. Yao, Two-step preparation of hierarchical porous carbon from KOH-activated wood sawdust for supercapacitor, Mater. Chem. Phys. 238 (2019) 121956, https://doi.org/10.1016/j.matchemphys.2019.121956.
[52] Y. Dall'Agnese, M.R. Lukatskaya, K.M. Cook, P.L. Taberna, Y. Gogotsi, P. Simon, High capacitance of surface-modified 2D titanium carbide in acidic electrolyte, Electrochem. Commun. 48 (2014) 118–122, https://doi.org/10.1016/J.ELECOM.2014.09.002.